Supporting Information

On-chip Vectorial Structured Light Field Manipulation by Inverse design

Wang Zijia[1†], Kunhao Lei[1†], Shenglong Yang[1†], Mengxue Qi[1,] Jieren Song[1], Yuting Ye[2], Hui Ma[1], Yiting Yun[1],Qiwei Zhan[1], Da Li[1], Shixun Dai[3], Baile Zhang[4], Xiaoyong Hu[5], Lan Li[2], Erping Li[1*], Hongtao Lin[1,6*]

[1]*State Key Laboratory of Brain-Machine Intelligence, Key Laboratory of Micro-Nano Electronics and Smart System of Zhejiang Province, College of Information Science and Electronic Engineering, Zhejiang University, Hangzhou 310027, China.*

[2]*Key Laboratory of 3D Micro/Nano Fabrication and Characterization of Zhejiang Province, School of Engineering, Westlake University, Hangzhou 310024, China.*

[3]*Laboratory of Infrared Materials and Devices, Ningbo University, Ningbo 315211, China.*

[4]*Division of Physics and Applied Physics, School of Physical and Mathematical Sciences, Nanyang Technological University, Singapore 637371, Singapore.*

[5]*State Key Laboratory for Mesoscopic Physics, Frontiers Science Center for Nano-optoelectronics, School of Physics, Peking University, Beijing 100871, China.*

[6]*MOE Frontier Science Center for Brain Science & Brain-Machine Integration, Zhejiang University, Hangzhou 310027, China.*

Corresponding author. Email: hometown@zju.edu.cn, liep@zju.edu.cn

†*These authors contributed equally to this work.*

Section S1. On-chip structured light

The capability and functionality of an optical system ultimately rely on how precisely one can control the available degrees of freedom of light, including its spatial distribution, temporal waveform, and polarization state [1-3]. In this context, structured light broadly refers to optical fields whose amplitude, phase, and/or polarization exhibit engineered spatial textures, thereby enabling tailored light–matter interactions. A canonical example in free space is the family of orbital-angular-momentum (OAM) beams [4-8], which carry a helical phase profile and are commonly characterized by an integer topological charge.

However, generate guided vectorial fields that possess designed spatial phase or polarization textures within the waveguide remains an open problem. Most on-chip devices and circuits are designed around standard guided modes (e.g., conventional strip-waveguide eigenmodes) that do not explicitly encode rich spatial phase/polarization textures. To address this gap and focus our scope, we define on-chip structured light in this work as guided vectorial fields that exhibit specific phase/polarization patterns on a transverse plane, not the direct on-chip generation of free-space beams like OAM modes[9]. This tailored capability finds a natural platform in valley photonic crystals (VPCs)[10], whose topological interface states can inherently host distinctive vectorial field textures tied to the valley degree of freedom.

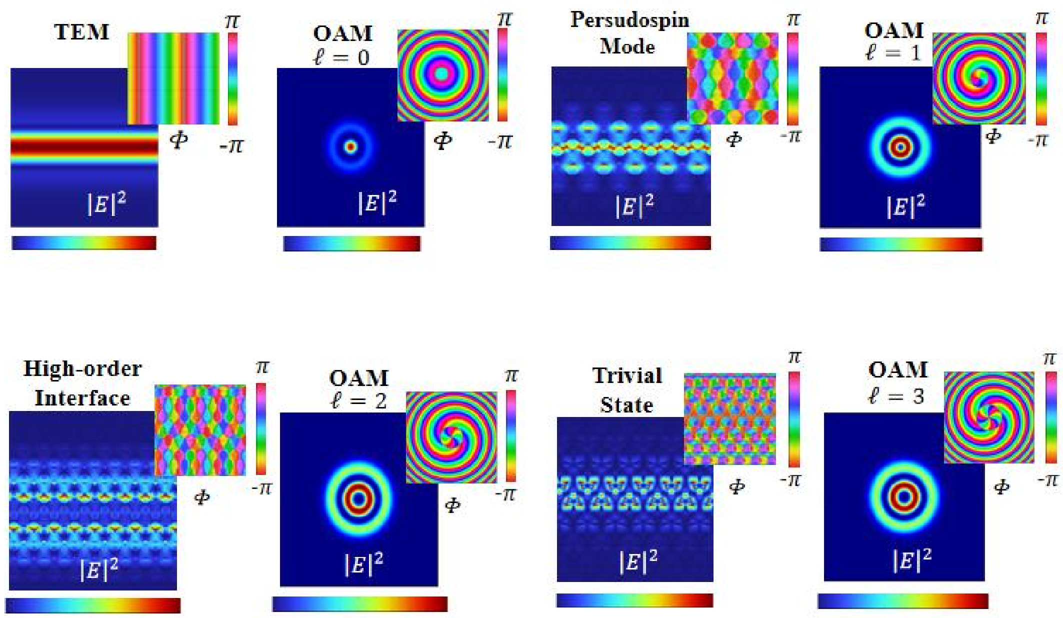

Fig. S1. Structured light and on-chip structured light.

For VPC interface states, the transverse field distribution can be understood through the coherent superposition of two time-reversal-related valley contributions. The guided field on the observation plane can be written as a superposition of Bloch-state components associated with the two valleys[11]:

$$\mathbf{E}(\mathbf{r})=a\mathbf{u}_K(\mathbf{r})e^{i\mathbf{K}\cdot\mathbf{r}}+b\mathbf{u}_{K'}(\mathbf{r})e^{iK'\cdot\mathbf{r}}, \tag{S1.1}$$

where $\mathbf{u}_K$ and $\mathbf{u}_{K'}$ are the periodic parts of the Bloch modes, and K and K' represent a pair of (nearly) degenerate valley states at the interface. Under this near-degeneracy, one can define valley pseudospin eigenstates as $\pm\pi/2$-phase-shifted superpositions:

$$|\psi_\pm\rangle=\frac{1}{\sqrt{2}}\left(|K\rangle\ \pm i\left|K'\right\rangle\right). \tag{S1.2}$$

This complex superposition naturally leads to rotating/chiral phase textures and spatially varying vector-field patterns on the transverse plane, forming a physically meaningful notion of structured fields in an integrated guided-wave setting.

A useful (but carefully bounded) analogy exists with classical free-space structured-light theory [12]: vortex-carrying Laguerre-Gaussian (LG) modes can be synthesized from two orthogonal HermiteGaussian (HG) modes via a ± i superposition, e.g.

$$\mathrm{LG}_{\pm1}\propto\mathrm{HG}_{10}\pm i\mathrm{HG}_{01}. \tag{S1.3}$$

Here, the key point is the shared mathematical mechanism: structured phase patterns can emerge from a complex superposition of orthogonal components. In our VPC case, the $\pm i$ superposition of valley components plays an analogous role in producing structured phase/polarization textures for guided fields on chip.

We emphasize, however, that this analogy should not be interpreted as a one-to-one identification between on-chip topological interface fields and free-space OAM beams. In free space, an OAM mode is typically associated with a global topological charge defined over an unbounded transverse plane. By contrast, VPC interface states are Bloch-type guided fields whose phase textures are strongly shaped by the lattice-scale harmonics and the band/interface configuration. As a result, the phase singularities or local phase-circulation features observed within/around a unit cell represent localized structured-field signatures rather than a global OAM charge.

Finally, the “order” intuition can be extended beyond the lowest-order examples. In free space, increasing the OAM index typically increases the complexity of phase winding and spatial structure. Analogously, higher-order photonic-crystal interface states (or different operating points across an edge-state band) can exhibit increasingly intricate unit-cell-scale phase/polarization textures (e.g., multi-lobed patterns or multiple localized phase-circulation features). This analogy offers a useful conceptual bridge between free-space structured beams and on-chip guided topological fields. By recasting on-chip vectorial field textures within a structured-light language (phase/polarization textures formed via coherent superposition), it provides a unified viewpoint for formulating target-driven synthesis and transformation of complex vectorial fields in integrated photonics. We expect this perspective to open up new routes for designing multifunctional on-chip devices that harness structured phase and polarization degrees of freedom, in close analogy to the rich toolbox developed in free-space structured-light optics.

Section S2. Quantum-state-inspired Hilbert-space representation of vectorial structured light

In classical optics, a Hilbert space provides a natural mathematical framework for representing electromagnetic fields as vectors and optical transformations as linear operators [13]. Any physically admissible optical field can be regarded as an element of a complex vector space spanned by a complete set of orthogonal basis functions. When equipped with an inner product, this vector space forms a Hilbert space, enabling rigorous treatment of field superposition, orthogonality, and linear transformations.

Within the Hilbert-space framework, a classical vectorial structured light field can be expressed using a quantum-state–inspired notation. This notation treats the classical field as a state vector, allowing different degrees of freedom to be described in a unified linear-algebraic form. The introduction of a Hilbert space does not imply quantum behavior, rather, serves purely as a mathematical container for classical electromagnetic fields, analogous to its widespread use in Fourier optics, mode theory, and polarization optics. For on-chip guided-wave photonic systems with a fixed propagation direction, the electromagnetic field possesses two independent transverse polarization degrees of freedom. Accordingly, we construct the total Hilbert space as the tensor product

$$\mathscr{H}=\mathscr{H}_{\mathrm{space}} \otimes \mathscr{H}_{\mathrm{pol}}\,, \tag{S2.1}$$

where $\mathscr{H}_{\mathrm{space}}$ is spanned by spatial sampling states on a chosen transverse observation plane, and $\mathscr{H}_{\mathrm{pol}}$ is spanned by an orthonormal Cartesian polarization basis $\{\hat{e}_x,\hat{e}_y,\hat{e}_z\}$. Under this construction, let E(r)denote the complex vectorial electric field obtained from full-wave electromagnetic simulations. By selecting an orthonormal basis spanning the relevant spatial and polarization degrees of freedom, the optical field can be written in the quantum state[14]:

$$|E\rangle = \sum_{i=1}^{N} \sum_{j\in\{x,y,z\}} c_{ij} |r_i\rangle \otimes |p_j\rangle . \tag{S2.2}$$

Here, $|r_i\rangle$ denotes the basis state associated with the i-th spatial sampling point on the transverse observation plane, and $|p_j\rangle$ denotes the orthonormal polarization basis state corresponding to the Cartesian unit vector $\hat{e}_j$. The complex coefficients c_{ij} encode the amplitude and phase of the field in the corresponding spatial–polarization basis.

This expression adopts the mathematical form of a quantum state but describes a purely classical electromagnetic field. The term quantum-state–inspired refers solely to the use of state-vector notation within a Hilbert space, not to any quantum optical effect.

Section S3. On-chip structured-light manipulation as an inverse design problem

The full evolution of an electromagnetic field governed by Maxwell's equations occurs in an infinite-dimensional function space. Direct manipulation of this space is neither necessary nor practical for inverse design. To enable numerical implementation, we introduce a projection operator $\mathscr{M}$, which maps the continuous vectorial field to a finite-dimensional representation by sampling the field on selected transverse observation plane(s):

$$\mathscr{M} : \mathbf{E}(\mathbf{r}) \longrightarrow \mathbf{C} \in \mathbb{C}^{N\times d}. \tag{S3.1}$$

Here, N denotes the number of spatial sampling points and $d=3$ is the dimensionality of the polarization subspace corresponding to $\{\hat{e}_x,\hat{e}_y,\hat{e}_z\}$, i. e. , the sampled components (E_x,E_y,E_z). Provided that the sampling window covers the dominant energy region and the sampling density satisfies the constraints of Maxwell's equations, this projection is information-equivalent to the original continuous field. This procedure establishes a finite-dimensional Hilbert space suitable for numerical modeling while preserving the essential physics of the electromagnetic field.

The projection operator $\mathscr{M}$ introduced in Eq. (S3.1) serves only to define a finite-dimensional representation of continuous vectorial electromagnetic fields by sampling them on selected transverse observation plane(s). The physical action of the device itself is governed by Maxwell's equations and can be described, in the continuous function space, by a linear field-evolution operator $\mathscr{L}$ that maps an input field to an output field. Specifically, for linear, passive media under fixed frequency, the input-output relation can be written as

$$\mathbf{E}_{\text{out}}(\mathbf{r})=(\mathscr{L}\mathbf{E}_{\text{in}})(\mathbf{r}). \tag{S3.2}$$

To connect this continuous operator to the finite-dimensional representation used in inverse design, we introduce (possibly distinct) projection operators $\mathscr{M}_{\text{in}}$ and $\mathscr{M}_{\text{out}}$ which map the continuous fields on the input and output observation planes to their discretized coefficient representations:

$$\mathbf{c}_{\text{in}}=\mathscr{M}_{\text{in}}[\mathbf{E}_{\text{in}}(\mathbf{r})], \quad \mathbf{c}_{\text{out}}=\mathscr{M}_{\text{out}}[\mathbf{E}_{\text{out}}(\mathbf{r})], \tag{S3.3}$$

where $\mathbf{c}_{\text{in}}$ and $\mathbf{c}_{\text{out}}$ are the finite-dimensional coefficient vectors (or vectorized coefficient arrays) collecting the sampled complex amplitudes over the chosen spatial-polarization basis.

In addition, we define a synthesis (reconstruction/embedding) operator $\mathscr{M}_{\text{in}}^{\dagger}$ that maps a finitedimensional coefficient vector back to a continuous field within the chosen input basis, i.e.,

$$\mathbf{E}_{\text{in}}(\mathbf{r})=\mathscr{M}_{\text{in}}^{\dagger}\mathbf{c}_{\text{in}}. \tag{S3.4}$$

Substituting Eqs. (S3.2) and (S3.4) into Eq. (S3.3) yields

$$\mathbf{c}_{\text{out}}=\mathscr{M}_{\text{out}}[\mathscr{L}\mathbf{E}_{\text{in}}(\mathbf{r})]=\mathscr{M}_{\text{out}}\mathscr{L}\mathscr{M}_{\text{in}}^{\dagger}\mathbf{c}_{\text{in}}. \tag{S3.5}$$

Therefore, we could define the transmission matrix T as the matrix representation of the continuous Maxwell operator $\mathscr{L}$ under the chosen input/output projection and synthesis operators:

$$T \triangleq \mathscr{M}_{\text{out}}\mathscr{L}\mathscr{M}_{\text{in}}^{\dagger}. \tag{S3.6}$$

With this definition, the discretized input-output relation immediately takes the standard linear form

$$c_{\text{out}}=Tc_{\text{in}}, \tag{S3.7}$$

which is the finite-dimensional operator equation used throughout this work for transmission matrix construction and inverse design.Notably, the transmission matrix T defined in Eqs. (S3.6)-(S3.7) is fully determined by the device physics captured by the continuous Maxwell operator $\mathscr{L}$, which in turn is uniquely specified by the spatial distribution of the dielectric permittivity $\varepsilon(\mathbf{r})$ (and permeability $\mu(\mathbf{r})$, if applicable). In frequency domain and for linear, source-driven problems, the electric field inside the design region satisfies the operator form of Maxwell's equations

$$A(\varepsilon)\mathbf{E}(\mathbf{r})=\mathbf{b}, \tag{S3.8}$$

where $A(\varepsilon)$ denotes the Maxwell operator, e.g. $A(\varepsilon)=\nabla\times\mu^{-1}\nabla\times-\omega^2\varepsilon(\mathbf{r})$ under standard assumptions, ω is the angular frequency, and $\mathbf{b}$ represents the excitation (equivalently defined by input ports/modes). The device input-output mapping (and hence the scattering/transfer behavior) is a linear functional of the solution $\mathbf{E}(\mathbf{r})$, obtained by projecting the simulated fields onto the chosen output basis. Therefore, the induced finite-dimensional operator T can be viewed as a deterministic functional of the permittivity distribution:

$$T\equiv T(\varepsilon)=\mathcal{M}_{\mathrm{out}}\,\mathscr{L}(\varepsilon)\mathcal{M}_{\mathrm{in}}^{\dagger}\,. \tag{S3.9}$$

Since $|E_{\mathrm{in}}\rangle$, $|E_{\mathrm{out}}\rangle$ denotes the finite-dimensional field coefficients under the chosen spatial–polarization basis, we may identify

$$c_{\mathrm{in}}\triangleq|E_{\mathrm{in}}\rangle,\ c_{\mathrm{out}}\triangleq|E_{\mathrm{out}}\rangle. \tag{S3.10}$$

Therefore, Eq. (S3.7) can be equivalently written as

$$|E_{\mathrm{out}}\rangle=T|E_{\mathrm{in}}\rangle. \tag{S3.11}$$

Consequently, structured-light manipulation can be formulated as a inverse design problem: given a desired mapping between input and target output field states, we seek a permittivity distribution $\varepsilon(\mathbf{r})$ within a prescribed design region such that $T(\varepsilon)$ matches the target mapping under Maxwell-consistent constraints. In this way, arbitrary vectorial structured-light manipulation can be realized on chip by tailoring the device permittivity distribution.

Section S4. Computational representation of the spatial-polarization bases

In this work, the spatial-polarization basis is defined using a transverse sampling-point representation. Specifically, one transverse cross-section along the propagation direction is selected as the output observation plane, corresponding to the physically relevant device interface where the structured-light field is specified and evaluated. On this plane, the vector electric field is spatially sampled on a fixed grid $\{\mathbf{r}_i\}_{i=1}^{N}$.

The polarization basis is chosen as an orthonormal set of transverse components(e.g., E_x,E_y,E_z). Under this construction, the vectorial field on the observation plane is represented by a finite-dimensional complex coefficient matrix $E \in \mathbb{C}^{N\times d}$, with d=3 polarization degrees of freedom. Accordingly, the input and output dimensions satisfy $N_{in} = N_{out} = N\times d$. Here, N is set by the sampling window and the sampling pitch aligned with the simulation mesh.

The selection of the spatial-polarization basis follows three practical criteria:

1. Energy coverage: the sampling window fully covers the dominant energy region of the output field (including the spatial localization of guided or edge states, when applicable) to avoid truncation errors;

2. Sampling resolution: the sampling pitch matches the numerical mesh used in the full-wave simulations and is verified by mesh/sampling refinement until key performance metrics (e.g., insertion loss and extinction ratio) converge, ensuring that the discretized representation is information-equivalent to the continuous field; In practice, we adopted a sampling density of 20 nm×20 nm×50 nm, which has been validated to resolve the dominant spatial features of the field while maintaining computational efficiency[19,20].

3. Consistency: the same observation plane(s) and sampling grid are used for all wavelengths and throughout all optimization iterations, ensuring a consistent definition of the transmission matrix and reproducible optimization results.

Section S5. Topology inverse-design algorithm and iterative update mechanism

In this work, the device is obtained by a standard gradient-based topology-optimization workflow implemented in Ansys/Lumerical lumopt. The goal is to find a physically realizable permittivity distribution ε(r) inside a prescribed design region such that the resulting device best matches the desired transmission-matrix constraint (Fig. S1). Below we summarize the algorithmic steps, including the optimization loop, spatial filtering/projection, continuation strategy, and the design-for-manufacturing (DFM) stage.

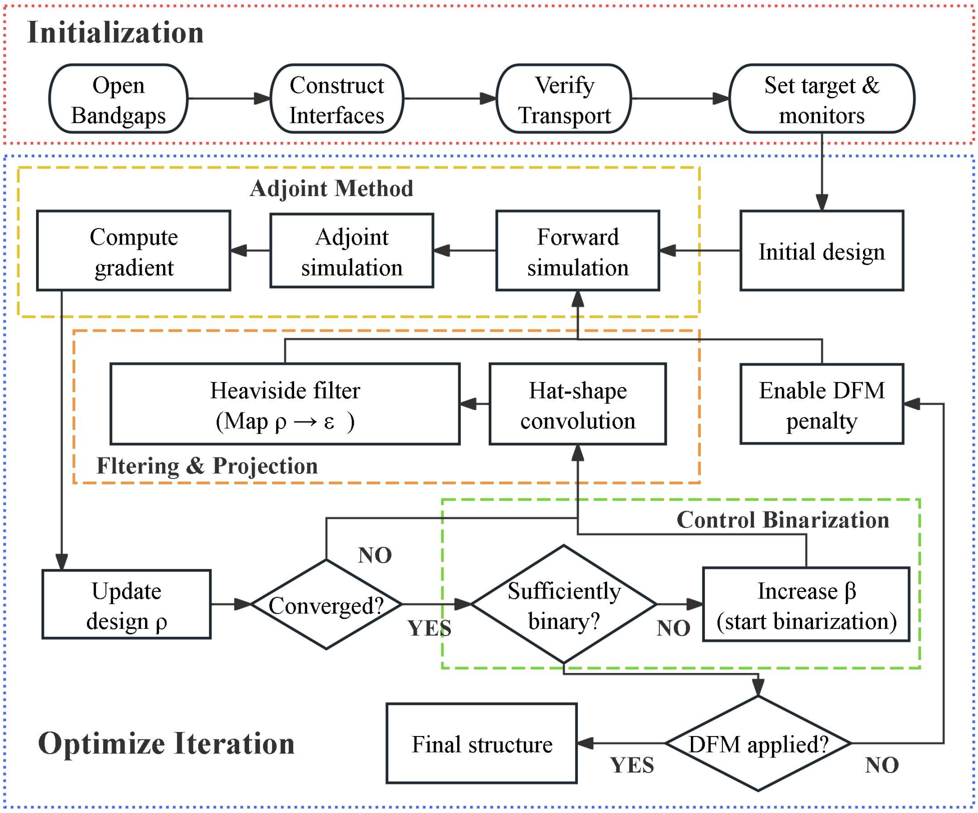

Fig. S2. Workflow of the inverse-design algorithm

Design parameterization

The design region is discretized into N pixels/mesh cells. Each cell is assigned a continuous density variable $\rho_i \in [0,1]$. In the greyscale phase, ρ_i is mapped to a local permittivity value through a linear interpolation between the cladding and core materials:

$$\varepsilon_i(\rho_i) = \varepsilon_{\min} + \rho_i(\varepsilon_{\max} - \varepsilon_{\min}) \tag{S5.1}$$

Thus, the set of density variables $\rho = \{\rho_i\}_{i=1}^{M}$ serves as the optimization variable.

S3.2 Per-iteration loop: forward simulation, adjoint gradient, and optimizer update

At each iteration k_k, the current density field $\rho^{(k)}$ is mapped to a permittivity distribution and evaluated by:

1. Forward simulation: a full-wave simulation computes the electromagnetic fields and the figure of merit (FOM) associated with the target transmission-matrix mapping.

2. Adjoint simulation: an adjoint run provides the gradient of the FOM with respect to the design parameters. A key advantage of the adjoint method is that the gradient can be obtained with only two simulations per iteration (one

forward + one adjoint), regardless of the number of design variables.

3. Gradient-based update: a gradient-based optimizer (as in lumopt) updates the density field:

$$\tilde{\rho}^{(k+1)}=\rho^{(k)}-\alpha^{(k)}\nabla_{\rho}\mathrm{FOM}, \tag{S5.2}$$

where $\alpha^{(k)}$ denotes the step size determined internally by the optimizer. After this update, additional processing steps (filtering + projection) are applied to enforce manufacturable patterns, as described below.

The termination condition labeled "Converged?" in the Manuscript Fig.2b corresponds to the optimizer's stopping criteria (e.g. sufficiently small improvement of the FOM, small gradient norm, or reaching the maximum number of iterations).

Spatial filtering: top-hat convolution

Pure topology optimization can introduce many fine features that are difficult to fabricate. Therefore, after each optimizer update, the design field is spatially smoothed by a circular top-hat convolution filter with radius *R* (denoted as filter_R in lumopt). Intuitively, this step suppresses sharp corners, small holes, and isolated islands, and promotes a minimum length scale in the evolwing structure.

Projection (Heaviside-type mapping) and binarization

After filtering, a projection step is applied to push the continuous greyscale distribution toward a near-binary two-material layout. We adopt a standard Heaviside-type mapping with threshold η and projection strength β, which converts the filtered density into a projected permittivity:

$$\varepsilon_i=\varepsilon_{min}+\frac{\tanh(\beta\eta)+\tanh\left(\beta(\rho_i-\eta)\right)}{\tanh(\beta\eta)+\tanh(\beta(1-\eta))}(\varepsilon_{max}-\varepsilon_{min}). \tag{S5.3}$$

Here, η controls the transition threshold (biasing the mapping toward ε_{min} or ε_{max}), while β controls how steeply the mapping approaches a step function. In the greyscale phase, β is kept small (approximately linear mapping). In the binarization phase, β is gradually increased, which progressively drives the design toward a nearly binary pattern.

Continuation scheme for β

Increasing β makes the projection sharper and therefore typically causes transient changes in the FOM (often observed as abrupt "spikes" or "peaks" in the optimization curve). This can be viewed as a controlled perturbation of the optimization landscape. To ensure stable convergence, the algorithm performs a number of regular optimization iterations after each increment of β, allowing the design to adapt to the new projection strength. In lumopt, the number of iterations between successive β-increments is controlled by a continuation schedule (e.g, continuation_max). The decision box "Sufficiently binary?" in the flowchart corresponds to checking whether the permittivity distribution has reached an acceptably near-binary state under the current β; if not, β is increased and the optimization continues.

Design-for-manufacturing (DFM) stage

Even after filtering and projection, topology-optimized patterns may contain sub-resolution features that violate process design rules. To improve manufacturability, we optionally introduce a DFM phase[18] by adding a penalty term to the FOM that penalizes violations of a prescribed minimum feature size constraint. In lumopt, this is enabled by specifying a non-zerol min_feature_size (with the typical constraint R< min_feature_size <2R ; setting it to zero disables the DFM phase). This penalty suppresses ultra-fine or fragile structures, enhancing robustness to fabrication imperfections, typically at the cost of a modest reduction in the ideal simulated performance. The flowchart branch "DFM applied?" indicates whether this penalty stage is enabled to finalize a fabrication-friendly design.

Summary

Overall, the iterative update mechanism can be summarized as:

$$\rho^{(k)} \xrightarrow{\text{forwsrd + sdjoint}} \nabla_{\rho}\text{FOM} \xrightarrow{\text{optimizer}} \tilde{\rho}^{(k+1)} \xrightarrow{\text{filter + projection}} \rho^{(k+1)},$$

with a continuation schedule on β for binarization, and an optional DFM penalty stage to enforce minimum feature sizes.

Reference

1. Zang W B, Yuan Q, Chen R, et al. Chromatic dispersion manipulation based on metalenses Advanced Materials 32(27): 1904935, (2020)

2. Yu N F, Capasso F. Flat optics with designer metasurfaces. Nature Materials, 13: 139-150, (2014)

3. Zou X J, Zheng G G, Yuan Q, et al. Imaging based on metalenses. PhotoniX, 1(1): 2., (2020)

4. Berry M V 2000 Making waves in physics: three wave singularities from the miraculous 1830s Nature 403 21

5. Ndagano, B., Nape, I., Cox, M. A., Rosales-Guzman, C. & Forbes, A. Creation and Detection of Vector Vortex Modes for Classical and Quantum Communication. J. Lightwave Technol. 36, 292–301 (2018).

6. Willner, A. E. et al. Optical communications using orbital angular momentum beams. *Adv. Opt. Photonics*. 7: 66 (2015).

7. Curd, A. *et al.* Construction of an instant structured illumination microscope. *Methods* 88, 37–47 (2015).

8. York, A. G. *et al.* Instant super-resolution imaging in live cells and embryos via analog image processing. *Nat Methods* 10, 1122–1126 (2013)

9. Yang, Y., Ren, Y.-X., Chen, M., Arita, Y. & Rosales-Guzmán, C. Optical trapping with structured light: a review. *Adv. Photon.* 3, (2021).

10. E.Yablonovitch, Photonic band-gap structures. J. Opt. Soc. Am. B 10, 283 (1993)

11. J. W. Goodman, Introduction to Fourier Optics, 3rd ed. (Roberts & Company Publishers, 2005).

12. Rubinsztein-Dunlop, H. et al. Roadmap on structured light. J. Opt. 19, 013001 (2017).

13. Nape, I. et al. Revealing the invariance of vectorial structured light in complex media. *Nat. Photonics*. 16: 538-546 (2022)

14. Mao, D. et al. Generation of polarization and phase singular beams in fibers and fiber lasers. Adv. Photon. 3, (2021).

15. Liu, M. et al. Broadband generation of perfect Poincaré beams via dielectric spin-multiplexed metasurface. Nat Commun 12, 2230 (2021).

16. Ndagano, B., Nape, I., Cox, M. A., Rosales-Guzman, C. & Forbes, A. Creation and Detection of Vector Vortex Modes for Classical and Quantum Communication. J. Lightwave Technol. 36, 292–301 (2018).

17. Zhou, M. et a. "Minimum length scale in topology optimization by geometric constraints", Comput. Methods in Appl. Mech. Eng 293, 266-282 (2015)

18. Lin, X. et al. Compact Mid-Infrared Chalcogenide Glass Photonic Devices Based on Robust-Inverse Design. Laser & Photonics Reviews 17, 2200445 (2023).

19. Wei, M. et al. Inverse design of compact nonvolatile reconfigurable silicon photonic devices with phase-change materials. Nanophotonics 13, 2183–2192 (2024).